

Hydrodynamic Investigation of USP Dissolution Test Apparatus II

GE BAI,¹ PIERO M. ARMENANTE,¹ RUSSELL V. PLANK,² MICHAEL GENTZLER,² KENNETH FORD,² PAUL HARMON²

¹Department of Chemical Engineering, New Jersey Institute of Technology, Otto H. York Newark, 323 M. L. King Boulevard, Newark, New Jersey 07102-1982

²Merck & Co., West Point, Pennsylvania 19486

Received 18 April 2006; revised 5 July 2006; accepted 18 August 2006

Published online in Wiley InterScience (www.interscience.wiley.com). DOI 10.1002/jps.20818

ABSTRACT: The USP Apparatus II is the device commonly used to conduct dissolution testing in the pharmaceutical industry. Despite its widespread use, dissolution testing remains susceptible to significant error and test failures, and limited information is available on the hydrodynamics of this apparatus. In this work, laser-Doppler velocimetry (LDV) and computational fluid dynamics (CFD) were used, respectively, to experimentally map and computationally predict the velocity distribution inside a standard USP Apparatus II under the typical operating conditions mandated by the dissolution test procedure. The flow in the apparatus is strongly dominated by the tangential component of the velocity. Secondary flows consist of an upper and lower recirculation loop in the vertical plane, above and below the impeller, respectively. A low recirculation zone was observed in the lower part of the hemispherical vessel bottom where the tablet dissolution process takes place. The radial and axial velocities in the region just below the impeller were found to be very small. This is the most critical region of the apparatus since the dissolving tablet will likely be at this location during the dissolution test. The velocities in this region change significantly over short distances along the vessel bottom. This implies that small variations in the location of the tablet on the vessel bottom caused by the randomness of the tablet descent through the liquid are likely to result in significantly different velocities and velocity gradients near the tablet. This is likely to introduce variability in the test. © 2007 Wiley-Liss, Inc. and the American Pharmacists Association *J Pharm Sci* 96:2327–2349, 2007

Keywords: dissolution; testing; pharmaceutical testing; USP dissolution test apparatus; hydrodynamics; laser doppler velocimetry, LDV; computational fluid dynamics, CFD; coning

INTRODUCTION

Solid dosage forms, such as tablets, are a convenient way of administering drugs to patients. Upon ingestion, tablets disintegrate into smaller fragments in the body compartment

where absorption by the body is initiated, typically in the stomach or the upper intestine. These fragments dissolve in the digestive juices and can become absorbed by an epithelial layer such as the lining of the upper intestine. This complex *in vivo* process is routinely simulated in *in vitro* dissolution tests mandated by the food and drug administration (FDA) and specified in United States pharmacopoeia (USP).

Dissolution testing is routinely carried out in the pharmaceutical industry to determine the rate of dissolution of solid dosage forms. In addition to

Correspondence to: Piero M. Armenante (Telephone: 973-596-3548; Fax: 973-596-8436; E-mail: piero.armenante@njit.edu)

Journal of Pharmaceutical Sciences, Vol. 96, 2327–2349 (2007)
© 2007 Wiley-Liss, Inc. and the American Pharmacists Association

being routinely used by pharmaceutical companies to demonstrate adequate drug release *in vivo* (through *in vivo/in vitro* (IVIVC) correlation), *in vitro* dissolution testing is used to assist with formulation design, process development, and especially the demonstration of batch-to-batch reproducibility in production. Dissolution testing is one of the several tests that pharmaceutical companies typically conduct on oral dosage formulations (e.g., tablets) to determine compliance and to release products for distribution and sales.

Although the USP lists several different dissolution test apparatuses,¹ most dissolution tests are currently conducted with USP Dissolution Test Apparatus I and II. The USP Dissolution Test Apparatus II is the most commonly and widely used apparatus specified by the USP, and it is the focus of the hydrodynamic study presented in this work. The dimensions, characteristics, and operating conditions of USP Dissolution Test Apparatus II are detailed by the USP,¹ and all users must conform to these prescriptions when conducting dissolution tests.

The USP Dissolution Test Apparatus II comprises a glass vessel and an agitation system. The glass vessel is a cylindrical glass tank with a hemispherical bottom, and a working volume of 900 mL (Fig. 1a). The agitation system consists of a two-blade paddle impeller mounted on a shaft centrally located in the vessel and profiled to follow

the hemispherical portion of the vessel. In the industrial practice, replicate dissolution tests are typically conducted in parallel using commercially available systems containing six or more individual USP Dissolution Test Apparatus II units (Fig. 1b). These systems allow the agitation system (motor and impellers) to be lifted above the rack holding the vessels, as shown in this figure, in order to prepare the system for the actual test. Each vessel is filled with a prescribed amount of a fluid simulating gastric or intestinal fluids, and maintained at constant temperature of 37°C by either a water bath or a heating jacket.

The test consists of lowering the agitation system so that the paddles reach their predetermined location inside the vessels, as required by the USP, starting the agitation so that the paddles rotate at 50 rpm (in some instances 75 or 100 rpm), adding a single dosage form unit, such as a tablet, to each vessel simultaneously, drawing liquid samples over time from a prescribed location within the vessel, analyzing the drug concentration in each sample, and determining the dissolution profile over time. These profiles must be within a predefined range, and cannot differ significantly from the dissolution profile that the drug manufacturer has initially submitted to the FDA when the drug was approved. Any dissolution profile that is found to be statistically different, according to a predefined criterion,² from the

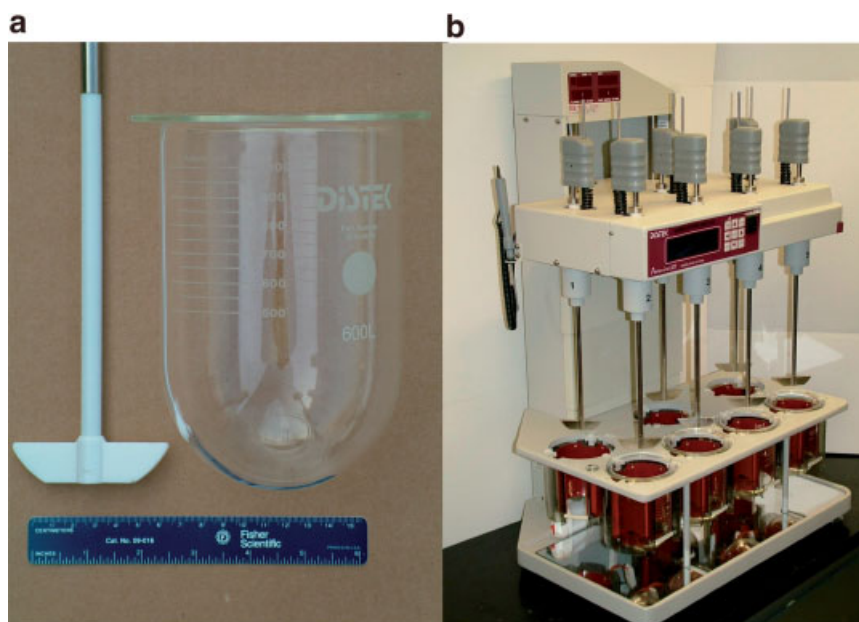


Figure 1. USP Dissolution Testing Apparatus II: (a) paddle impeller and glass vessel; and (b) typical commercial dissolution testing systems containing seven Apparatus II units (Distek Premiere 5100 Bathless Dissolution System).

reference profile established for that dosage form implies failure of the test and non-compliance of the production batch being tested. When this occurs, the batch cannot be released for commercialization and it is often disposed of. The cost of such failure is often significant given the typical high value of the product.

The USP Dissolution Test Apparatus II has been used in the pharmaceutical industry for decades, since this test was first officially introduced almost 30 years ago.³ Nevertheless, and despite its widespread use in the industry, dissolution testing remains susceptible to significant error and test failures. A review of the literature shows that there have been numerous reports describing high variability of test results,^{4–11} even when the so called “calibrator tablets” (i.e., tablets manufactured for the sole purpose of testing the proper operation of the dissolution test equipment) are used.^{5,7,10,12,13} Failures linked to dissolution testing resulted in 47 product recalls during the period 2000–2002, representing 16% of non-manufacturing recalls for oral solid dosage forms.^{14–16} Irrespective of the underlying causes (such as incorrect use of the equipment or deviation of dissolution profile from the standard caused by incorrect tablet formulation) failed dissolution tests can result in product recalls, costly investigations, potential production delays, which, in turn, can have a significantly negative financial impact.

Some of the same studies have indicated that the hydrodynamics of Apparatus II appears to play a major role in the poor reproducibility of dissolution testing data and the inconsistency of dissolution results. This is hardly surprising considering that Apparatus II is a small, un baffled vessel with a hemispherical bottom provided with a slowly rotating paddle, in which a tablet (or another dosage form) is dropped. This system can be expected to be associated with a complex hydrodynamics resulting in fluid velocities whose directions and intensities are highly dependent on the location within the vessel. To complicate the issue farther, tablets have often been reported to land at different locations at the bottom of the vessel after they are dropped in the vessel at the beginning of a test, making the dissolution process even more susceptible to hydrodynamic factors.

Until recently, limited information has been available on the hydrodynamics of the dissolution apparatus and the effects of operating and geometric variables on the velocity distribution in the system. Such information is critical to

advance the fundamental understanding of the dissolution rate process, enhance the reliability of dissolution testing, and eliminate artifacts associated with test methods, especially since dissolution measurements have often been reported to be inconsistent and poorly reproducible. A literature review shows that a few investigators have conducted hydrodynamic studies. Bocanegra et al.⁹ measured the flow field by laser Doppler anemometry (LDA), the first experimental measurement of this kind in dissolution vessels. These researchers generated data only for very limited regions of the vessel. More recently, Kukura et al.¹² obtained experimental flow patterns using particle image velocimetry (PIV) and laser-induced fluorescence (LIF), and computed the velocity flow field using computational fluid dynamics (CFD). However, they presented very limited quantitative comparison between the experimental data and the predictions. Other researchers also made an effort to determine the flow field inside the USP Apparatus II vessel through CFD. Kukura et al.¹⁷ and Baxter et al.¹³ predicted the flow pattern and shear effects with CFD. McCarthy et al.^{18,19} predicted the flow field with CFD and compared the CFD predictions with the limited experimental results from previous research.⁹

This overview shows that our current knowledge on the hydrodynamics of dissolution testing systems is still greatly incomplete, and that there is a significant need for work aimed at fully quantifying the hydrodynamics in the USP Apparatus II both computationally and experimentally. Therefore, the primary objective of this work is to quantify the hydrodynamics in a standard USP II dissolution vessel by experimentally mapping (via laser Doppler velocimetry) and computationally predicting (via CFD) the velocity distribution inside the vessel under the typical operating conditions mandated by the dissolution test procedure. A detailed comparison of the numerical predictions against the experimental data is also provided, and it appears to be favorable.

EXPERIMENTAL APPARATUS AND METHOD

Dissolution Vessel and Agitation System

A standard USP Apparatus II dissolution vessel consisting of an un baffled, cylindrical, transparent, glass tank with a hemispherical bottom, and having an internal diameter, T , of 100.16 mm

and an overall capacity of 1 L was used in all experiments (Fig. 2a). The agitation system consisted of a standard USP II two-blade paddle impeller mounted on a shaft. The exact geometry of the impeller was obtained by measuring the actual dimensions with a caliper, which were found to be as follows: shaft diameter, 9.53 mm; length of the top edge of the blade, 74.10 mm; length of the bottom edge of the blade, 42.00 mm; height of the blade, 19.00 mm; and thickness of the blade, 5.00 mm. This impeller was provided by the Merck researchers and had a slightly larger diameter shaft at the blade, resembling a collar, as opposed to the uniform shaft diameter, including the portion at the blade, typical of the USP design. The radius of this collar was only 1.6 mm larger than that of the rest of the shaft. The experiments and the computational results were obtained with this impeller in order to insure exact conformity to the Merck system. However, the geometric differences between this system and the typical USP system are so minimal that the result obtained here are expected to be equally valid for the USP impeller with no collar.

Since only the hydrodynamics of the system was of interest here, the dissolution vessel and paddle were not assembled in a full dissolution system similar to that shown in Figure 1b. Instead, the impeller was connected to a 1/8-HP motor controlled by an external controller (G.K. Heller Corp, Model 202P6518) which was used here to rotate at

a constant agitation speed of 50 rpm, the conventional operating condition specified in the USP for the test. The corresponding impeller tip speed was 0.194 m/s and the impeller Reynolds number was 4939. The motor-impeller system was mounted on a bracket above the vessel so that the impeller was centered in the vessel and the impeller clearance off the vessel bottom was 25 mm, as mandated by USP. The vessel was filled with 900 mL of deionized water, as in the typical case for this test.

Laser-Doppler Velocimetry (LDV) System

Laser-Doppler velocimetry (LDV) is a non-intrusive experimental method used to determine the local velocity distribution (including its fluctuating component) in a fluid inside any transparent piece of equipment. LDV has been proved to be a very valuable experimental method in fluid mechanic studies and was extensively used by several investigators to quantify the flow characteristics of mixing vessels and reactors.^{20–23} In this project, a Dantec 55× series LDV apparatus (Dantec Measurement Technology USA, Mahwah, NJ) was used to determine the velocity flow field and turbulence intensity inside the vessel (Fig. 3). The LDV system comprised a 750 mW argon-ion laser (Ion Laser Technology, Inc.) producing a single multicolored laser beam passing through an optical filter to generate a monochromatic green beam (wavelength: 512 nm). The resulting beam passed through a beam

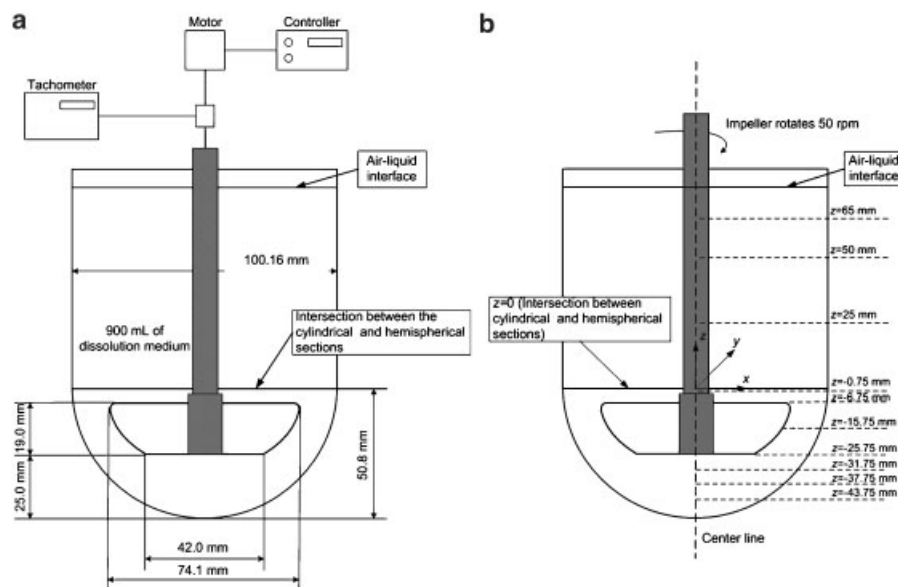


Figure 2. (a) Basic geometry of USP Dissolution Apparatus II vessel and impeller; and (b) iso-surfaces at different vertical positions.

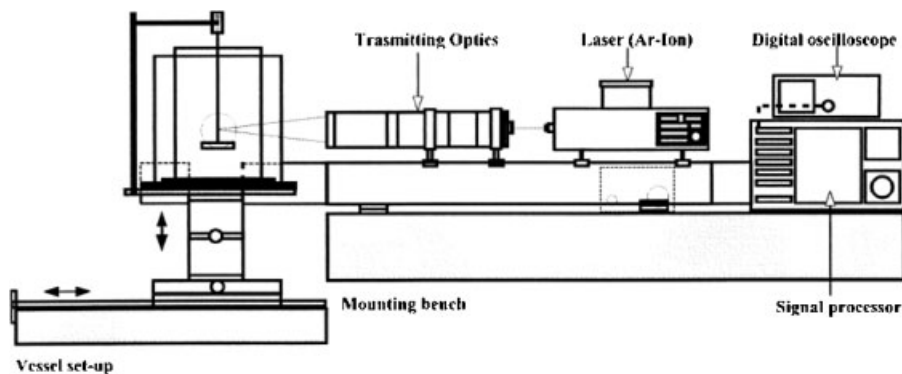


Figure 3. Laser-Doppler velocimetry (LDV) apparatus used in this work.

splitter from which two beams emerged, one of which was passed through a Bragg cell to lower the frequency by 40 MHz and distinguish between positive and negative velocity measurements. The beams then passed through a beam expander system and a final focusing lens with a focal length of 330 mm. This lens made the beams converge so that they intersected each other to form a small control volume in the interrogation region where the velocity was to be measured. In an actual measurement, the beams were made to converge inside the USP II vessel.

The USP II vessel was suspended from a bracket specifically built so that the vessel could be placed in an external Plexiglas square tank filled with water, in order to minimize optical distortion during LDV measurements. The water in the USP vessel was seeded with trace amounts of neutrally buoyant 1.5 μm silver coated particles (TSI, Inc., Minneapolis, MN) that could follow the fluid flow pattern very closely.

The motor-impeller-vessel assembly was mounted on an x-y-z traversing system that could position the vessel at any desired location in front of the LDV system, thus enabling the velocity to be measured anywhere in the vessel. The light scattered by the particles was collected by a photodetector assembly placed next to the tank at a 90° orientation with respect to the laser, and connected to a data acquisition system. The time interval for each measurement was typically 60 s. In most cases, some 600–2500 instantaneous velocity data points were collected at any location and for the selected velocity component, from which the local average velocity and turbulence intensity could be calculated. Data analysis was performed to generate the local velocity components in the direction parallel to that of the plane of the two laser beams. Appropriate rotation

of the laser beam assembly and translation of the vessel-motor assembly yielded the velocity components in all three directions at any location.

Ten iso-surfaces at different vertical (z) positions were selected along the height of the vessel where LDV velocity measurements were made (Fig. 2b). The horizontal plane where the cylindrical and hemispherical portions of the dissolution vessel intersect was taken as the iso-surface at $z=0$. The iso-surfaces at $z=-6.75$ mm, $z=-15.75$ mm, and $z=-25.75$ mm are the planes on which the top edge of the impeller blade, the middle of the impeller blade and the bottom edge of the impeller blade lie, respectively.

On the iso-surfaces above the impeller, LDV measurements were made at seven evenly spaced radial locations between the shaft and the vessel wall. However, because of the hemispherical shape of the vessel bottom and the presence of the impeller blades, fewer measurement locations were used in the impeller region and the bottom region. At each measurement location, three velocity components (tangential, axial, and radial) were obtained by LDV.

Numerical CFD Simulation

Numerical simulations of the velocity distribution and turbulence levels inside the USP II dissolution test apparatus were conducted using a commercial mesh generator (Gambit 2.1.6)²⁴ coupled with a computational fluid dynamic (CFD) package (Fluent 6.2.16).²⁵ The full 360° -tank geometry was incorporated in the simulations.

Mesh Generation and Mesh Quality

Figure 4 shows the mesh used in the CFD simulations. In order to save computation time

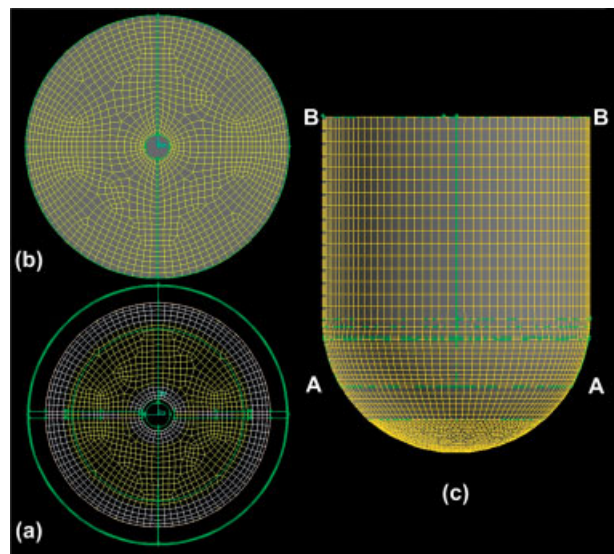


Figure 4. Mesh used in CFD simulation: (a) starting face on iso-surface at A-A; (b) top face on iso-surface at B-B; (c) axial, side view of mesh.

and effectively increase the simulation convergence, a structured Cooper-type hex mesh was created in the cylindrical portion of the vessel and in the upper section of the hemispherical vessel bottom above section A-A in Figure 4c. An unstructured, tetrahedral mesh was generated in the lower section of the hemispherical bottom to follow the curved shape more closely. Accordingly, the liquid volume was computationally partitioned into two sub-volumes. The meshes in each sub-volume were created starting from the same starting face (Fig. 4a), that is, the horizontal cross section of the vessel located where the lower edge of the impeller blade lies (section A-A in Fig. 4c). On this starting face, the curves resulting from the intersection of the horizontal plane with vertical solid surfaces such as the vessel wall (resulting in a circle) or the impeller blade edge (resulting in a rectangle) were identified. These curves were partitioned into small elements by specifying points on them from which the grid line started. This approach resulted in the generation of a larger number of smaller cells in the regions near the impeller and the tank wall in order to capture the steep velocity gradients in those regions. From the pre-meshed starting surface (Fig. 4a), a hex grid was generated with a Cooper-scheme approach, by extending and projecting the pre-meshed surface both upward, up to the liquid-air interface (Fig. 4b), and downwards, reaching down to the iso-surface 12.35 mm below

the lower edge of the impeller. A much finer tetrahedron mesh was created below this iso-surface, in order to capture the flow near the vessel bottom.

The mesh typically contained 80262 cells, 219590 faces, and 62472 nodes. Simulations with a mesh containing 258310 cells were also run, in order to evaluate the effect of grid number to the numerical solution. The two CFD predictions were not appreciably different. In fact, the results with the coarser mesh matched the LDV data marginally better.

Significant attention was paid to the generation of a high quality mesh, since this determined whether the simulation converged to a stable solution or not. The average EquiAngle Skew parameter (one of the most important parameters to determine the quality of the mesh) was typically in the range 0.3–0.4 (0-best; 1-worst) and was no larger than 0.809 for any individual cell. The size variation was very smooth in the complete domain. There was no hex cell with a high aspect ratio in the domain. The cell elements were fine enough to capture the high gradient of the geometry in the area of impeller blade and the bottom of the vessel.

CFD Approach

The control volume technique used by the solver involved the discretization of the computational domain into a finite number of contiguous control volumes. The conservation equations of mass and momentum were solved for each of these control volumes. All simulations were carried out on a Dell Precision 650 Workstation, equipped with two Intel XEON 2.8 Gigahertz processors and 2 gigabytes of random access memory (RAM). A typical simulation required 40000 iterations and about 30 h of CPU time to achieve conversion.

To account for the turbulent effects during the numerical simulations, CFD simulations were conducted using different turbulence models, that is, the $k-\omega$ model with low Reynolds number correction, RNG $k-\varepsilon$ model, and Realizable $k-\varepsilon$ model,^{26,27} or with no turbulence model at all, that is, assuming laminar flow. After preliminary results were obtained, as describe below, the $k-\omega$ model with low Reynolds number correction was selected and used throughout this work.

The standard $k-\omega$ model is an empirical model based on model transport equations for the turbulence kinetic energy (k) and the specific dissipation rate (ω), which can also be thought of as the ratio of ε to k .^{26,27} The $k-\omega$ model has been

modified over the years, and production terms have been added to both the k and ω equations, resulting in improved accuracy for free shear flows, lower sensitivity to boundary conditions, and better performance at lower Reynolds numbers. However, good convergence is not easily achieved. The governing equations for the standard k - ω model are as follows:

$$\frac{\partial}{\partial t}(\rho k) + \frac{\partial}{\partial x_i}(\rho k u_i) = \frac{\partial}{\partial x_j} \left(\Gamma_k \frac{\partial k}{\partial x_j} \right) + G_k - Y_k + S_k \quad (1)$$

$$\frac{\partial}{\partial t}(\rho \omega) + \frac{\partial}{\partial x_i}(\rho \omega u_i) = \frac{\partial}{\partial x_j} \left(\Gamma_\omega \frac{\partial \omega}{\partial x_j} \right) + G_\omega - Y_\omega + S_\omega \quad (2)$$

Because of the relatively low impeller rotational speed resulting in a low impeller Reynolds number ($Re = 4939$), large portions of the domain were dominated by transitional flow. A low Reynolds number correction of the standard k - ω model was applied to improve the velocity predictions in these flow regions.²⁵

Boundary Conditions and Frame of Reference

The no-slip condition in the appropriate frame of reference was assumed at all solid surfaces. The air–water interface was always assumed to be flat, since the agitation speed in this work was low enough (50 rpm) to prevent the formation of a vortex, as visually confirmed in the experiments. The air–water interface was modeled as a frictionless surface, and the normal gradients of all variables were zero at this interface.

A single reference frame approach was used in the CFD simulation in which the vessel wall was assumed to be rotating, and the impeller was stationary, although the appropriate body forces were included in the computation to account for the non-inertial characteristics of the rotating reference frame.

As mentioned above, the LDV apparatus can determine only the *average* velocity (separately for each component) at a given location, by measuring the *instantaneous* local velocities at that location over a period of time, typically 60 s, during which the impeller rotates but the measurement location relative to the (fixed) vessel does not. The instrument then determines the time-averaged velocity component at that location as well as other statistics. By contrast, the CFD simulations

produce time-invariant three-dimensional flow predictions where the velocities vary with position, including the azimuthal position. However, since the dissolution vessel is unbaffled, the CFD-predicted flow can also be viewed as a time-dependent flow in which the velocity at a given fixed location is a function of its azimuthal position relative to the rotating impeller. Therefore, in order to compare the LDV data with the CFD predictions, the CFD-predicted velocities at a given axial and radial position but different azimuth must be averaged along the circumference passing through that point in order to generate an average azimuthal velocity that can be compared with the time-averaged velocity of the LDV at the same axial and radial position.

In this work, for each velocity component, the CFD-predicted velocities at eight different azimuth positions at the same radial location on a given iso-surface were averaged to give a single value of the azimuth ensemble-averaged velocity component at that location. The ensemble-average local velocity component values so obtained could be compared with the time-averaged velocity measurements obtained experimentally with the LDV.

RESULTS

Selection of Turbulence Model for CFD Simulations

In a preliminary study, the results of simulations based on the use of two different turbulence models (the RNG k - ε model and the Standard k - ω model with Low Reynolds-Number correction) and those obtained with no turbulence model (i.e., laminar flow model) were compared with the LDV data collected on two different iso-surfaces ($z = 50$ mm, $z = -31.75$ mm) located above and below the impeller, respectively. Figure 5 shows that the results based on the turbulence models were of the same order of magnitude, indicating that this approach was somewhat robust.

The k - ω simulations were generally in better agreement with the LDV data than those with any other turbulence model or in the absence of any turbulence model. For example, the highest LDV tangential velocity at $z = 50$ mm was 43% of the impeller tip speed and was observed at relative radial position of 0.41. The k - ω simulations predicted that the peak tangential velocity was also 43% of the impeller tip speed, but at relative radial position of 0.47. By contrast, the RNG k - ε

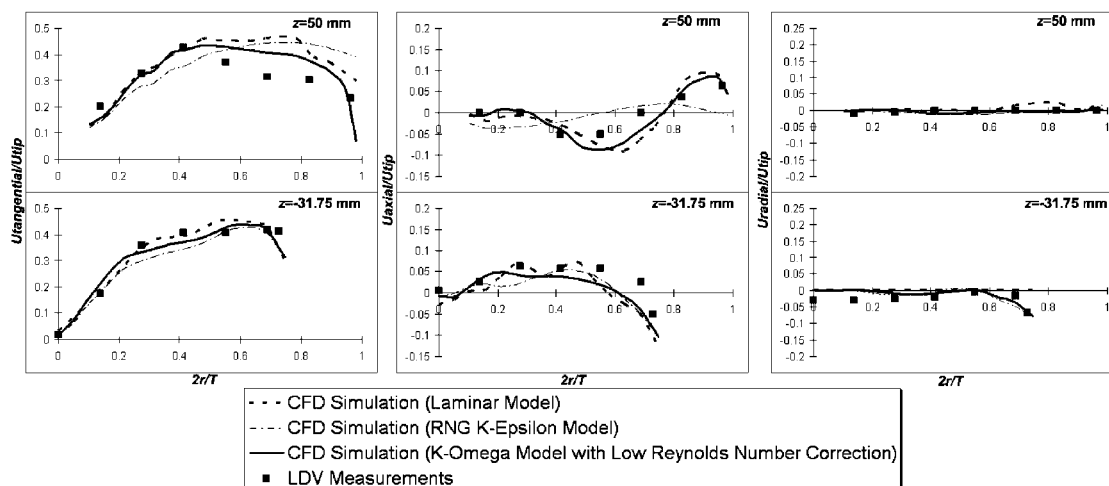


Figure 5. Comparison between experimental LDV velocity data and CFD predictions on iso-surface $z = 50$ mm and $z = -31.75$ mm using different turbulence models.

simulations predicted a peak velocity of 46% at relative radial position of 0.68. On the iso-surface at $z = -31.75$ mm, the agreement between the LDV data and the $k-\omega$ simulations was even better not only in the core region closer to the shaft, but also in the region extending beyond $2r/T = 0.27$, that is, where the velocity profiles flatten out.

As for the axial velocities, the shape and the magnitude of the velocity profiles predicted by $k-\varepsilon$ simulations were appreciably different from the LDV data, especially for $z = 50$ mm. The $k-\omega$ simulations predicted not only better velocity magnitudes but also shapes of the velocity profiles that were more similar to the LDV data.

Finally, the radial velocities on the iso-surface at $z = 50$ mm were all very small (less than 3.5% of the impeller tip speed), although the $k-\omega$ prediction were much closer to the LDV data. Similarly, for $z = -31.75$ mm, the $k-\omega$ model predicted a better shape of the velocity profile than RNG $k-\varepsilon$ model, even though the LDV data showed that the velocities were typically much smaller than 9% of the impeller tip speed.

In a separate series of simulations conducted for a slightly different geometry of the dissolution system than that used in this work another turbulence model was additionally tested, namely the Realizable $k-\varepsilon$ model. The results obtained with this model were only marginally better than those obtained with the standard $k-\varepsilon$ model (results not shown).

In the rest of the study, all simulations were conducted using the $k-\omega$ turbulence model with low Reynolds number correction. Similarly, all the

simulation results presented here were obtained using this model.

Velocity Distribution Profiles

Figures 6–8 show, respectively, the tangential, axial, and radial velocity profiles obtained from LDV measurements and the results of the CFD simulations based on the $k-\omega$ model with low Reynolds-Number correction. The LDV measurements on $z = -6.75$ mm and below were limited to locations between the hemispherical vessel wall and the impeller.

Figure 6 shows that all the tangential velocities, irrespective of the iso-surfaces where they were obtained, were oriented in the same direction as the impeller rotation, indicating a strong tangential flow, as in the case of other unbaffled systems.^{22,23,28–32} Everywhere in the vessel the experimental tangential velocities were always much stronger than the other components, with peak tangential velocities ranging between 40% and 50% of the tip speed on all iso-surfaces with the exception of the iso-surfaces at $z = -25.75$ mm and $z = -6.75$ mm, where the maximum velocity was 38%–36% of the tip speed, respectively. These velocity peaks were achieved at a radial distance $2r/T \approx 0.41$ on iso-surfaces at $z = -0.75$ mm and above; at a radial location very close to the blade tip on iso-surface at $z = -15.75$ mm (middle of the impeller blade); and at radial locations very close to the vessel wall on iso-surfaces at $z = -25.75$ mm and below. On the iso-surface at $z = -6.75$ mm, where the top edge of the impeller blade is located,

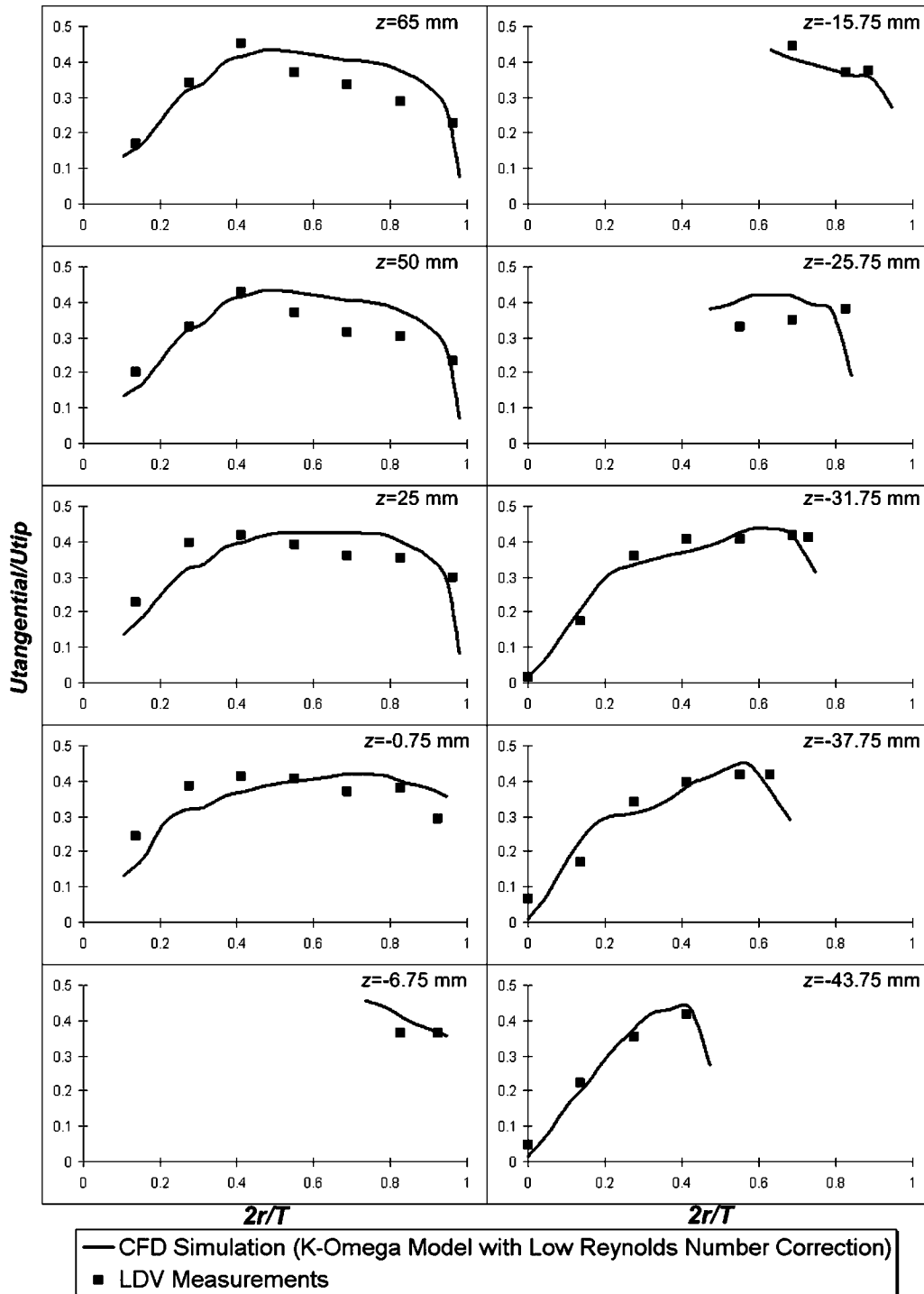


Figure 6. Comparison between LDV data and CFD predictions for tangential velocities on different iso-surfaces.

only two LDV measurements could be obtained. Significant although not complete agreement can be observed between the experimental data and the numerical results. Especially relevant is the good agreement between the LDV and CFD results

for the tangential velocities at or below the impeller. This is the most critical region for the operation of the USP II apparatus, because of the presence of the solid dosage form somewhere on the bottom of the vessel. This is also the most

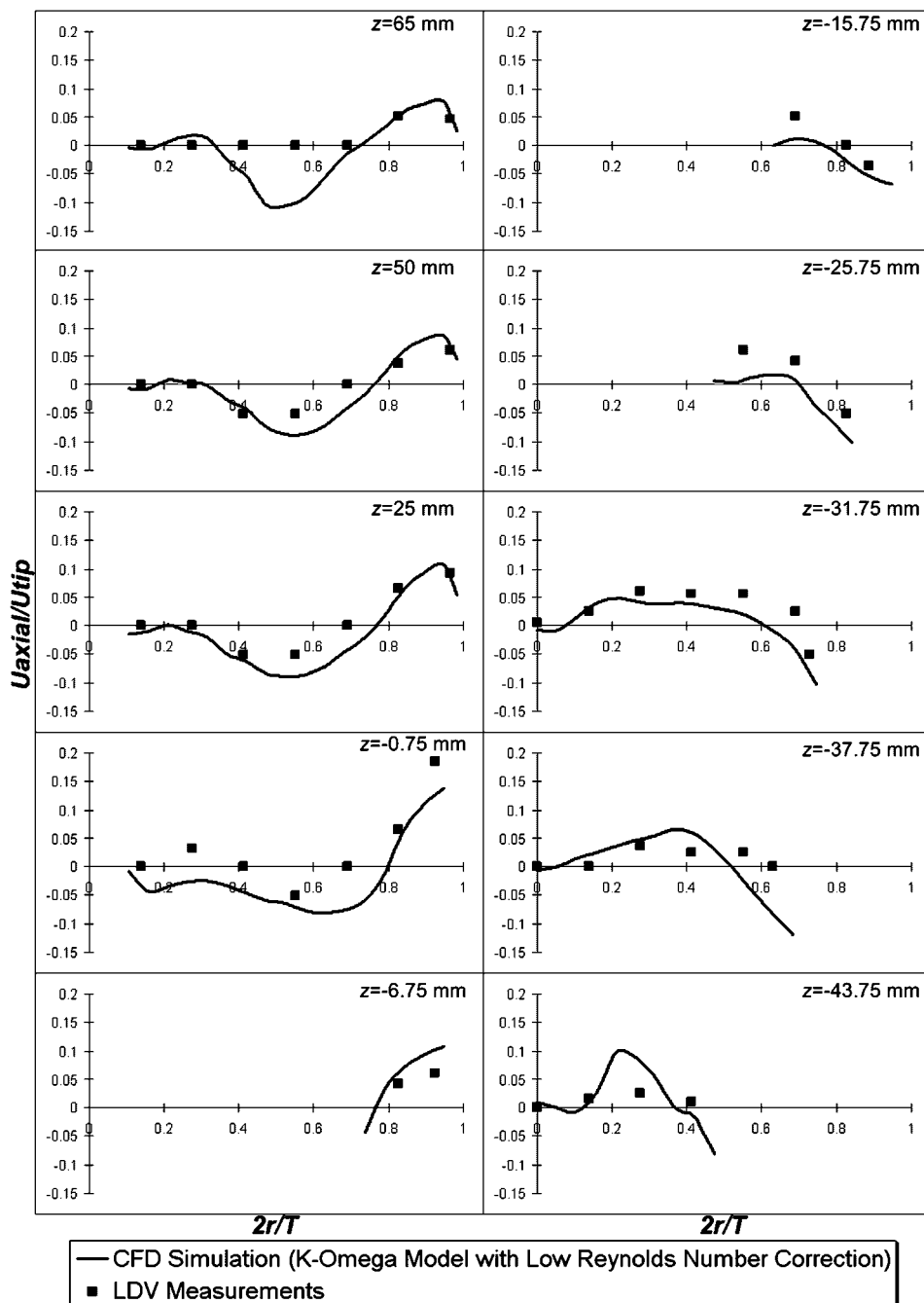


Figure 7. Comparison between LDV data and CFD predictions for axial velocities on different iso-surfaces. Positive values indicate upwards velocities.

difficult region where LDV measurements can be made because of the increasing curvature of the vessel with respect to the observation plane of the laser, that is, where the laser beams enter the vessel.

In the upper region of the vessel, that is, for $z \geq -0.75$ mm, the fluid in the inner core ($2r/T$

$T < 0.4$) rotates with the shaft in solid body rotation, as indicated by the linear increase of the velocity with $2r/T$ (Fig. 6). In the outer region ($2r/T > 0.4$), the velocity profiles are much flatter, and decrease slowly with the radial position before dropping rapidly at the tank wall, where the fluid velocity is expected to go to zero. LDV data could

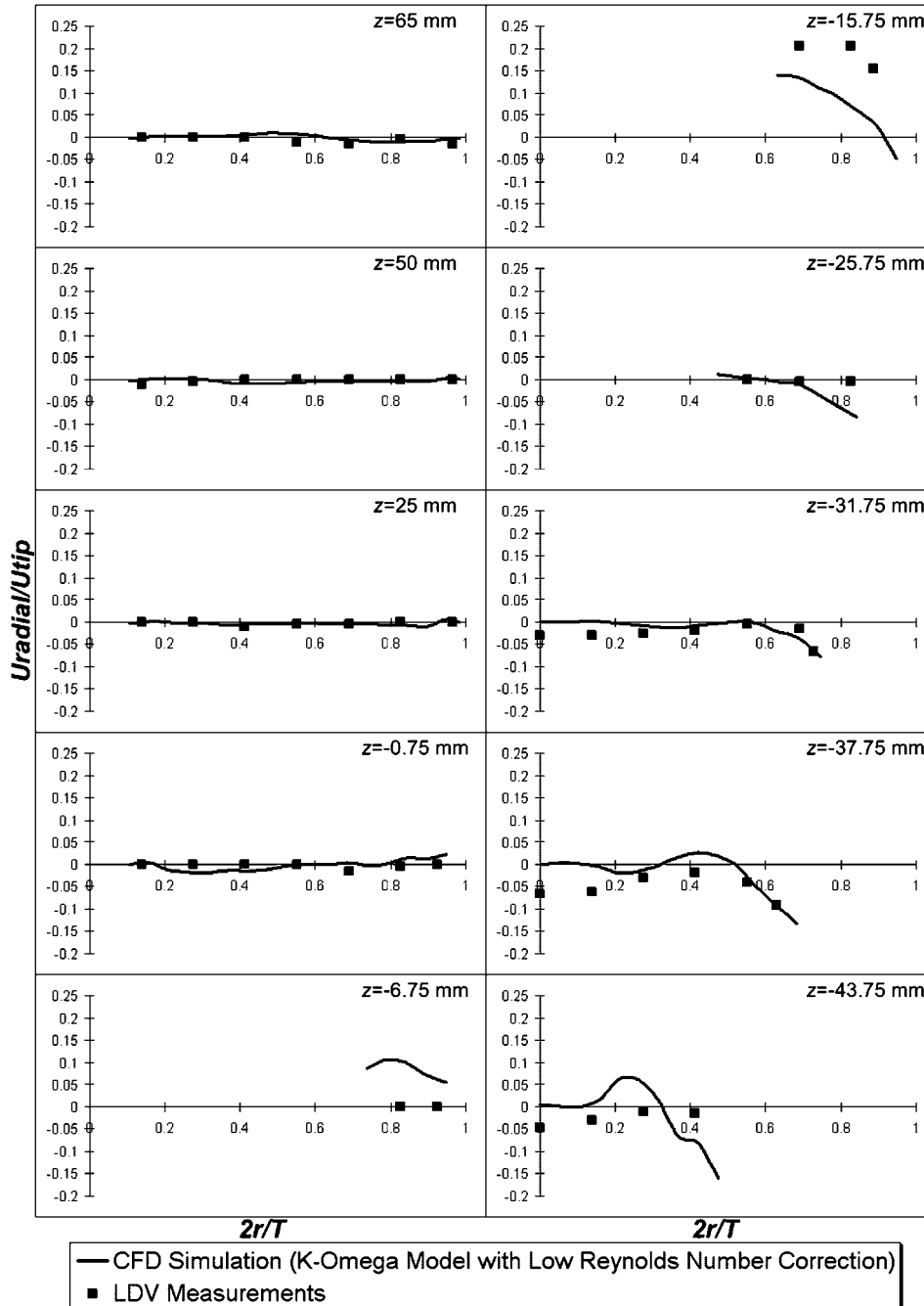


Figure 8. Comparison between LDV data and CFD prediction for radial velocities on different iso-surfaces. Positive values indicate velocities directed outwards, that is, away from the center of the vessel and toward the wall.

not be taken too close to the wall because of the optical distortion produced by the round glass wall.

On the iso-surface $z = -15.75$ mm, that is, in the middle of the impeller blade, the CFD profile matches closely the LDV measurements, showing

that the peak tangential velocity occurs near the impeller tip and decreases toward the wall. For $z = -6.75$ mm, where the top edge of the impeller blade lies, the CFD simulation shows that the tangential velocity is higher near the impeller blade than near the wall, while the LDV

measurements, although supporting the simulations, show a flat velocity profile and lower velocity magnitudes.

In the region below the impeller ($z = -25.75$ mm, $z = -31.75$ mm, $z = -37.75$ mm, $z = -43.75$ mm), both the LDV measurements and the CFD simulations show that the radial location where the peak velocity occurs is closer to the vessel wall, which is the opposite of what was observed in the region above the vessel (Fig. 6). This can be attributed to the proximity of the impeller and to the curvature of the vessel wall, creating a fluid region where the local tangential velocity follows more closely that of the impeller.

Figure 7 presents the results for the axial velocities. These velocities are relatively small compared to the tangential velocities, with the magnitude of the LDV axial velocities in the 0%–20% range of the tip speed, and those from the CFD simulations in the range at 0%–15% of the tip speed. On most iso-surfaces, the LDV measurements and CFD the simulations produced similar axial velocity profiles, although deviations occurred. In general, the CFD simulations predicted slightly higher absolute velocity magnitudes than the LDV measurements.

The velocities on the iso-surfaces above the impeller ($z = -0.75$ mm, $z = 25$ mm, $z = 50$ mm, $z = 65$ mm) or at the impeller top blade ($z = -6.75$ mm) are directed downwards near the center of the vessel and upwards near the vessel wall, creating a weak but clearly detectable top-to-bottom recirculation loop. The reverse is true in the region at or below the impeller ($z = -43.75$ mm, $z = -37.75$ mm, $z = -31.75$ mm, $z = -25.75$ mm, and $z = -15.75$ mm), where the flow near the wall is directed downwards. This is the result of the jet emanating radially from the impeller, impinging on the vessel wall, and then creating two weak recirculation loops above and below the impeller. This is typical of most radial (paddle-like) impellers, although in the USP II vessel the hemispherical bottom, the absence of baffles, and the relatively large size of the impeller with respect to the vessel diameter produce an even weaker flow in the region below the impeller.

On the iso-surface at $z = 65$ mm, the LDV measurements show a flat velocity profile with almost zero velocity magnitude in the region $0.13 < 2r/T < 0.68$, while the CFD simulations show negative velocities (Fig. 7). The discrepancy between these curves is an indication that the recirculation loop in the portion above the impeller actually “closes” below the iso-surface at

$z = 65$ mm (i.e., the flow converges back toward the shaft), while the CFD simulation predicts that this recirculation effect occurs at a higher vertical location. For $z = -25.75$ mm, $z = -6.75$ mm, $z = -0.75$ mm, $z = -15.75$ mm, the LDV and CFD profiles are similar, but translated vertically with respect to each other.

Finally, Figure 8 presents the results for the radial velocities. In the upper portion of the vessel (iso-surfaces at $z = -0.75$ mm, $z = 25$ mm, $z = 50$ mm, $z = 65$ mm), both the LDV measurements and CFD simulations show that the magnitude of the radial velocities is very small (less than 2.5% of the impeller tip speed), that is, a very weak radial flow. As for the impeller region, on the iso-surface at $z = -6.75$ mm, the LDV measurements show an almost zero radial velocity magnitude, that is, no radial flow. However, the CFD simulation shows positive (i.e., outward) radial velocities. For $z = -15.75$ mm, the reverse is true, that is, a positive radial velocity with a relatively high velocity magnitude of 22% of the impeller tip speed was measured with the LDV. This is reasonable because in this region the impeller blade should push the fluid toward the wall. The CFD simulation also shows positive velocities, but their magnitudes are only about half of the LDV measurements. All this means that the radial velocity is over predicted by CFD near the upper edge of the blade and is under predicted it in the middle of the impeller and near its lower edge, which implies that there is a small discrepancy between CFD predictions and LDV data about the exact location where the impeller produces the expected outward directed radial jet. Apparently, CFD predicts this point to be slightly higher than what actually observed experimentally. However, the phenomenon is adequately predicted by the CFD simulations. This change in radial flow must occur over a very small vertical distance in the small gap between the impeller blade and the vessel wall. Therefore, in this region, even a small error in the prediction of the location where this flow reversal occurs can produce a larger discrepancy with the experimental data.

Below the impeller, the radial velocity is typically negative, although still small. This is also expected since the flow must be negative near the vessel wall in this region, as the curvature of the vessel redirects the radial flow generated by the impeller inwards and toward the bottom of the vessel. This is what both the LDV measurements and CFD prediction show for lower iso-surfaces.

As already mentioned, difference between the slightly larger diameter shaft at the blade used in this work instead of the more commonly used uniform shaft diameter is so small that the results obtained here are expected to be equally valid for the USP impeller with no collar at the impeller blade.

Velocity Magnitude and Velocity Vectors

Figure 9 shows the contours of the CFD-predicted velocity magnitude on a vertical cross section

through the impeller shaft for different orientations of the impeller. Figure 10 presents the same contours plots of the velocity magnitude on iso-surfaces at different vertical (axial) locations. Additional plots show the velocity vectors on a vertical cross section through the impeller shaft at different orientations of the impeller (Fig. 11), an expanded view of the velocity vectors in impeller region (Fig. 12), an expanded view of velocity vectors near vessel bottom region for two different impeller orientations (Fig. 13), and, finally, the velocity vectors on the iso-surfaces at

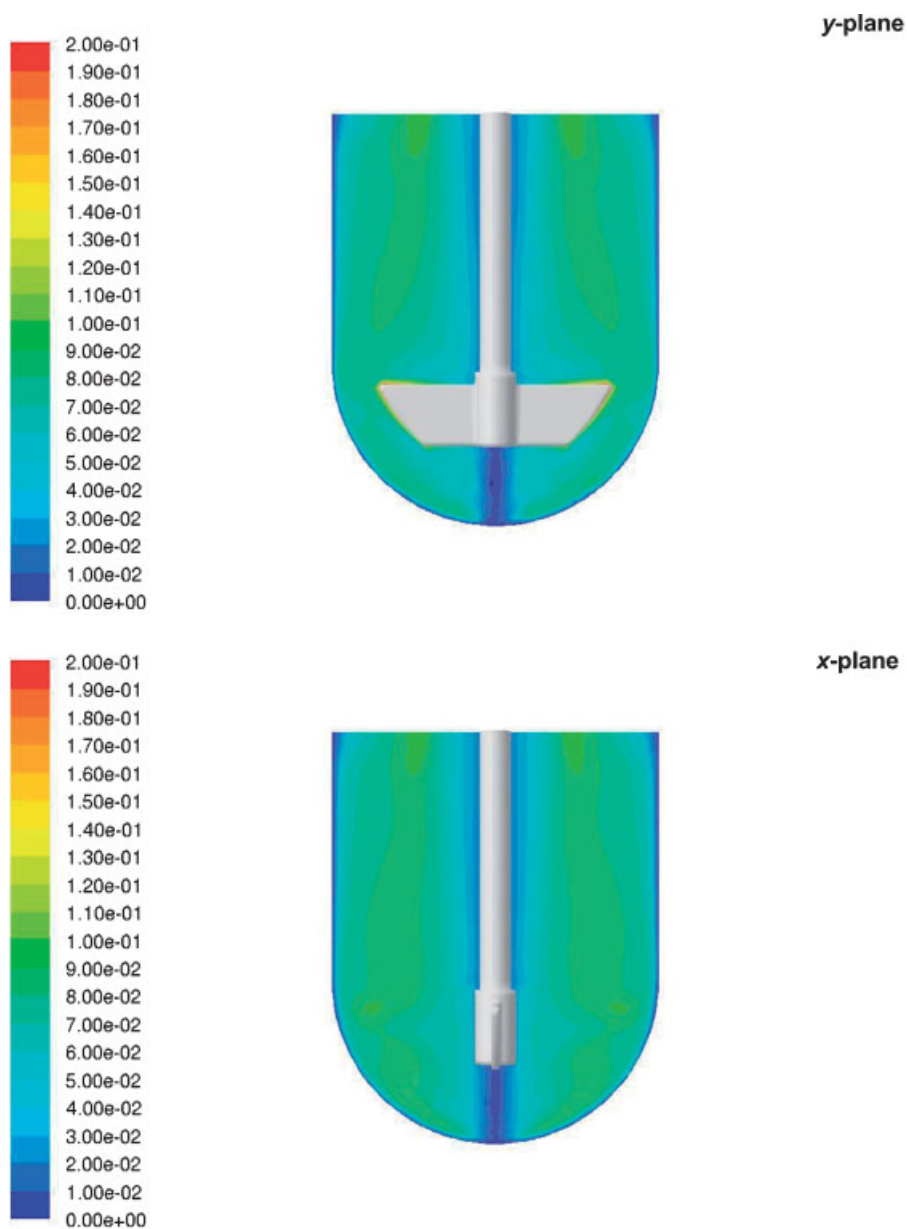


Figure 9. CFD predictions of the velocity magnitude on vertical cross sections through the impeller shaft for different impeller orientations (m/s).

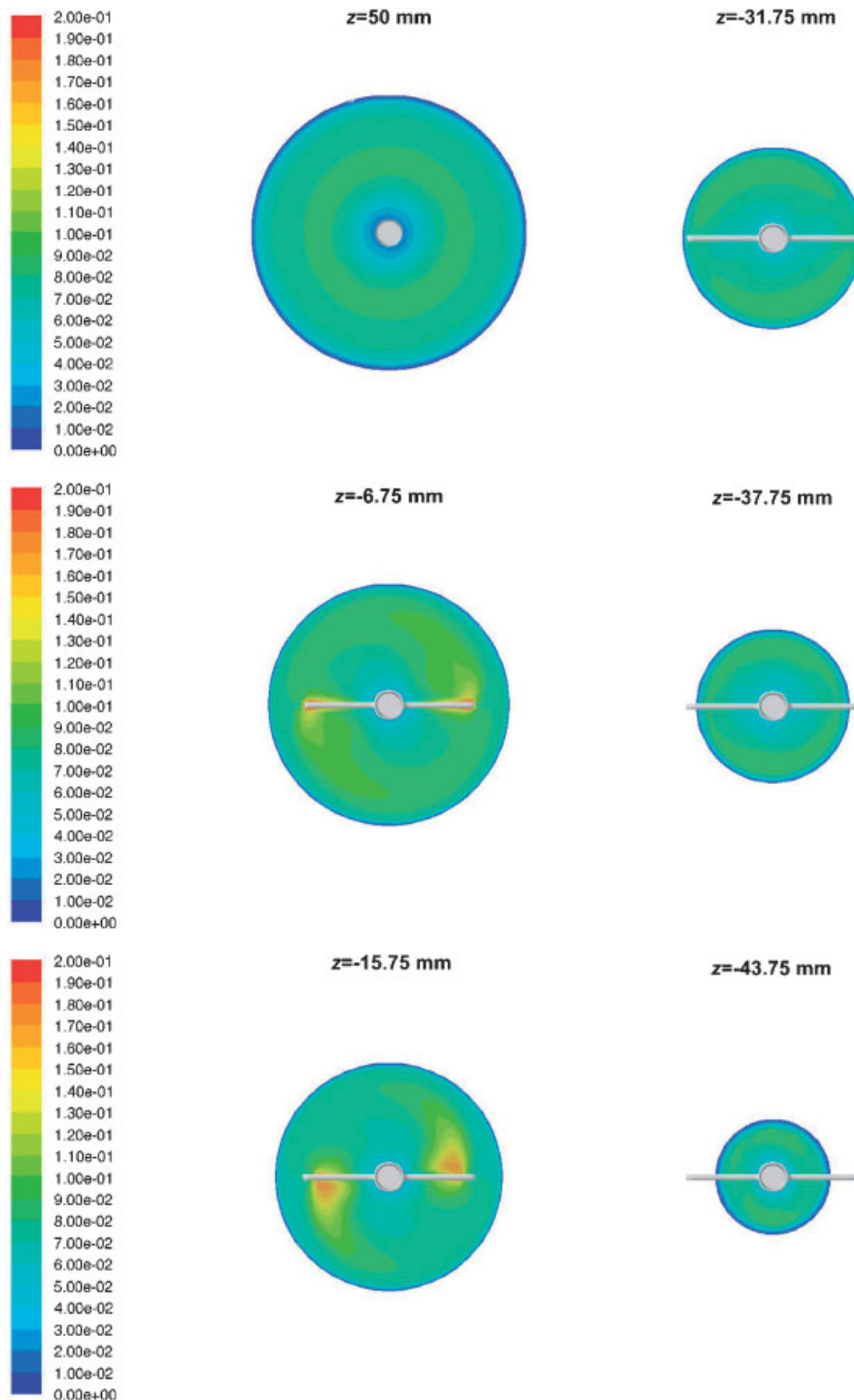


Figure 10. CFD predictions of velocity magnitude on different iso-surfaces (m/s).

different vertical locations (Fig. 14). In some of these figures, the greater vector density in the lower portion of the vessel is an artifact caused by the greater concentration of computational cells in that region (Fig. 4).

A full picture of the three-dimensional flow in the USP II vessel emerges by looking at all these figures and by combining them with the velocity profiles previously discussed (Figs. 6–8). The top portion of the vessel is dominated by a strong

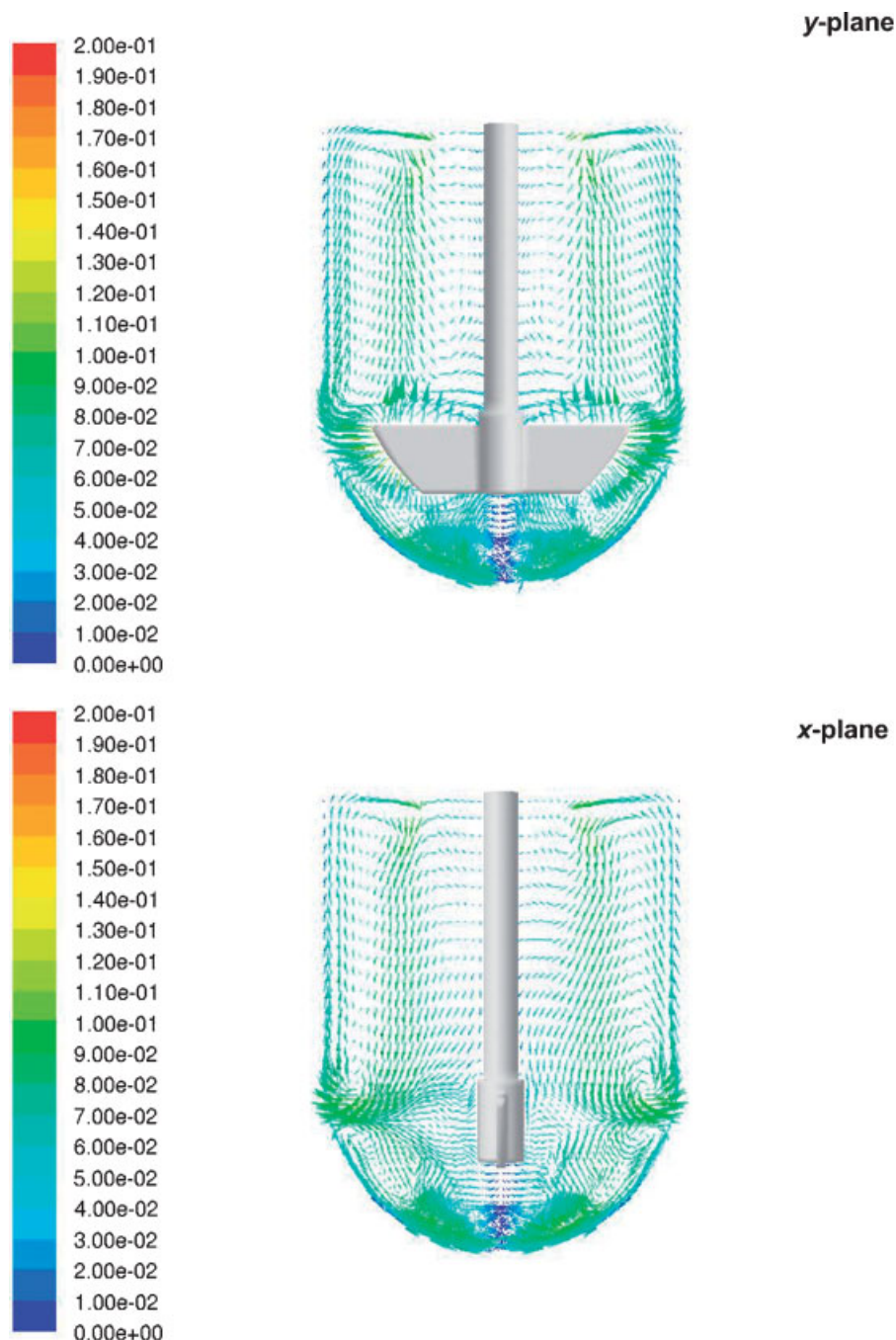


Figure 11. CFD predictions of velocity vectors colored by velocity magnitude on vertical cross section through the impeller shaft at different orientations (m/s).

tangential flow. A much weaker circulation loop caused by the impeller rotation is also present on the vertical cross section in the upper region of the vessel. The radial jet generated by the rotating impeller near the top edge of the blade impinges on the wall, producing an axial upward flow near the vessel wall. This flow is confined in the outer region of the vessel ($2r/T > \sim 0.7$; Figures 11 and 12). The

CFD simulation predicts that this loop closes very high in the tank, as indicated by the relatively stronger radial flow near the air–liquid interface (Fig. 11). In the middle inner core region above the impeller ($\sim 0.3 < 2r/T < \sim 0.7$), the flow is directed downwards. It should be remarked that this region does not extend all the way to the center of the vessel to include the shaft. Instead, the innermost

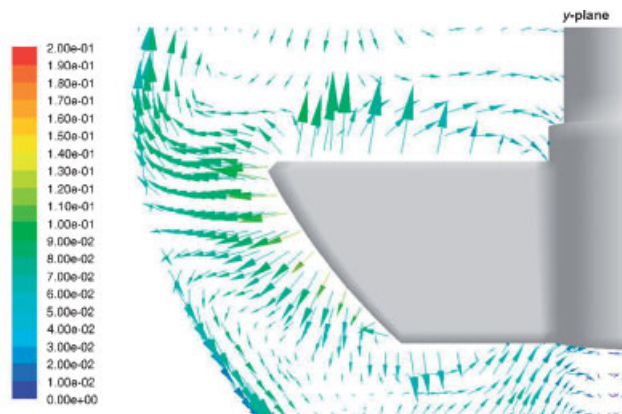


Figure 12. CFD predictions of velocity vectors colored by velocity magnitude on vertical cross sections through the impeller shaft for the impeller region (m/s).

core region ($2r/T < \sim 0.3$) is characterized by very low axial and radial velocities (Figs. 7 and 8) and by tangential velocities increasing proportionally to the radial position (Fig. 6). In other words, the inner core rotates almost as a solid body.

The fluid region around the impeller is obviously dominated by the impeller rotation (Fig. 12). The fluid velocity near the blade tip matches the tip speed. However, the fluid velocity decays rapidly, both radially and axially, away from the blade tip. For example, the velocities on the upper edge of the blade near the blade tip ($z = -6.75$ mm) are very similar to the tip speed, but the velocities on the iso-surface at $z = -0.75$ mm, which is only 6 mm above the top edge of the blade, show a significant decay in the velocity magnitude (Figs. 11 and 12). An even more

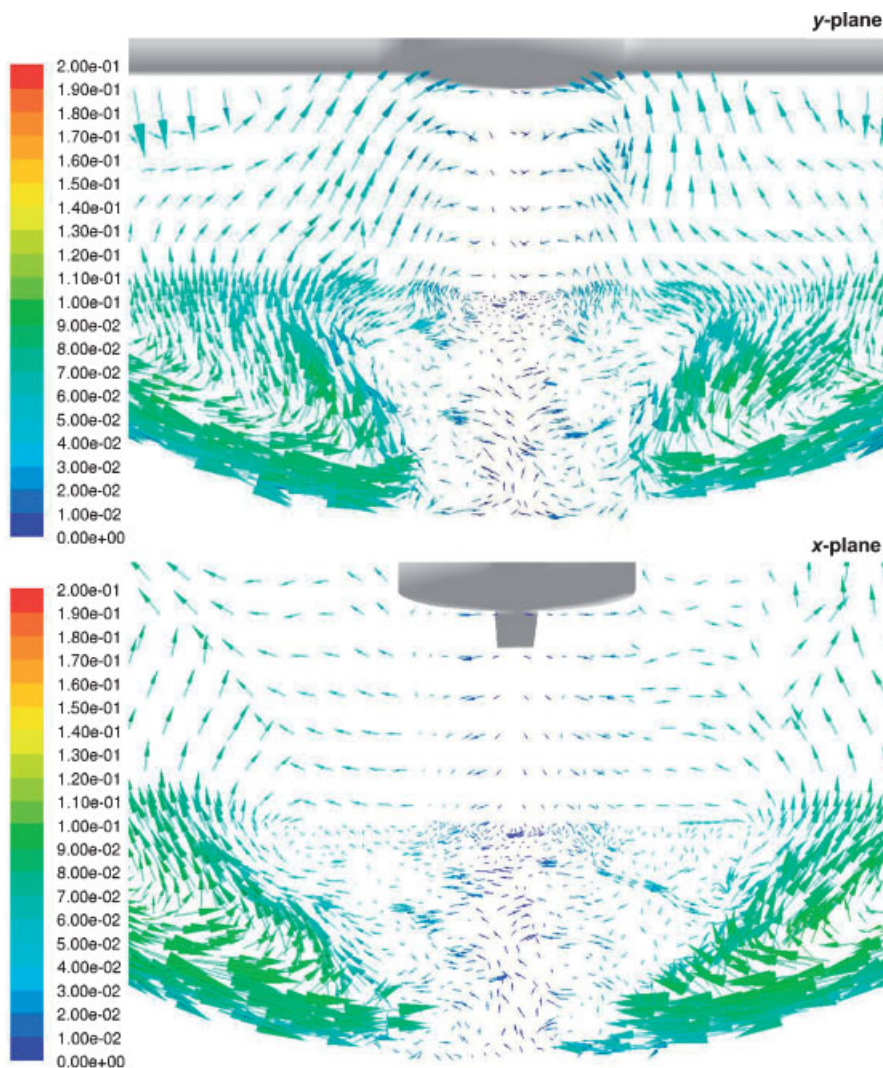


Figure 13. CFD predictions of velocity vectors colored by velocity magnitude on vertical cross section through the impeller shaft at different orientations, for the bottom region (m/s).

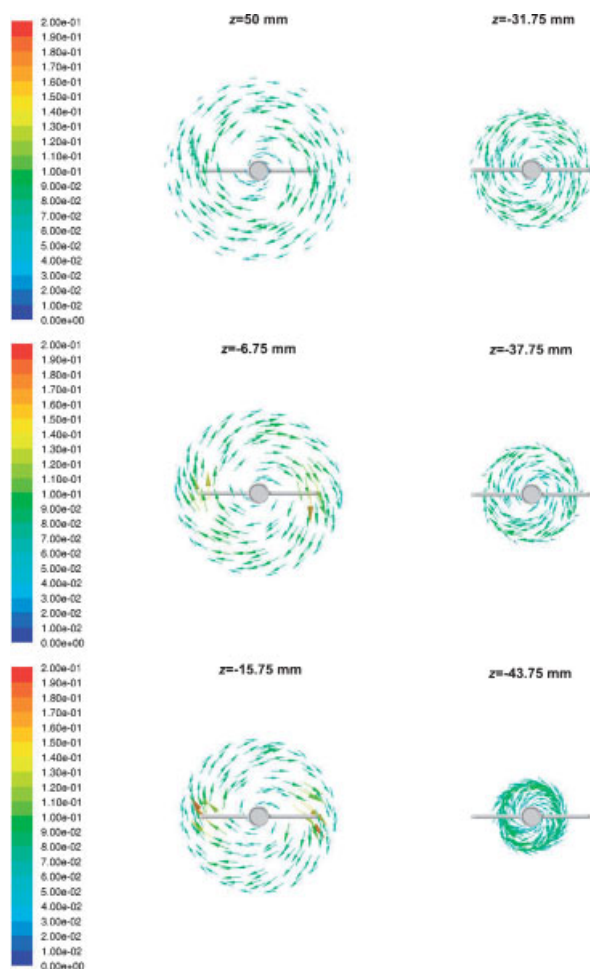


Figure 14. CFD predictions of velocity vectors colored by velocity magnitude on different iso-surfaces.

dramatic drop in velocity occurs in the radial direction, as it can be seen by moving away from the blade tip and towards the wall in Figure 12.

The radial jet generated by the impeller produces a complex flow in the gap between the blade tip and the vessel wall (Fig. 12). The radial flow is rapidly converted to a more axially oriented flow, which is predicted by the CFD to be directed upwards only near the top edge of the blade. Anywhere else in the gap, the flow is predicted to be oriented downwards. By looking at this figure, one can easily appreciate that even a minor error in the prediction of the vertical location where the flow switches direction from upwards to downwards can result in a significant discrepancy between the CFD results and the experimental LDV data. As already mentioned, this observation partially justifies the differences between the LDV and CFD results in this region.

The flow in the region below the impeller is the most complex and the most important for this work (Fig. 13 combined with Figures 6–8). These figures show that the flow is relatively strong in the tangential direction, even in the region below the impeller, but that the radial and axial components are generally weak, and are affected by the presence of a second vertical recirculation loop having a stronger pulsating component generated by the passing of the paddle. After the paddle has passed, the flow becomes extremely weak (Fig. 13).

The striking feature of the flow in the region below the impeller is that this vertical recirculation loop is not able to penetrate the inner core region located just at the center under the impeller (Figs. 9, 11 and 13). The net result is that the flow in this core is nearly stagnant in the vertical plane and it is dominated by weak tangential velocities (although stronger than the other components) on the order of 5% of the tip speed or less. This weakly swirling but otherwise nearly stagnant core region extends all the way from the vessel bottom to the lower edge of the impeller. As the impeller rotates, the stagnant core region expands (Fig. 13, y-plane) and contracts (Fig. 13, x-plane). The axial velocities change rapidly with time and location when moving across the vertical boundaries for this core region, while remaining very weak.

Figure 13 also shows that small changes in position near the bottom of the vessel are associated with large changes in the velocity magnitude. For example, by moving by a distance of only 2–5 mm, the velocity in the plane of the impeller can vary from near 0 to 1/3 of the tip speed, and possibly higher. It is obvious that such a change in local velocity can have a dramatic effect on the local mass transfer rate at a specific location on the surface of the tablet and hence on the local dissolution rate of a solid tablet. Even more importantly, the initial location of a dissolving tablet on the bottom of the vessel (e.g., inside the semi-quiescent region under the shaft or outside it) can produce significant differences in the velocity profiles and velocity gradients experienced by the tablet, with a possible significant impact on the dissolution or erosion rate.

The CFD simulations cannot be expected to provide a full description of such a complex flow, with such small velocities, in such a small region. However, the CFD results obtained here consistently capture the main features of the flow, including the fact that the flow under the impeller is dominated by a weak tangential flow and has

near zero radial and axial components. This is confirmed not only by the LDV results, but also by the robustness of the predictions in this region, which are relatively similar irrespective of the turbulence model used.

Turbulence Kinetic Energy (k) and Turbulent Dissipation Rate (ε)

Figures 15 and 16 show plots of the turbulence kinetic energy and turbulent dissipation rate, respectively, on vertical cross sections through the impeller shaft at different orientations. Appreciable turbulence levels and dissipation rates are present only in the impeller region, and especially near the blade tip. As the rotating impeller moves away from a given location in the impeller region, both turbulence and energy dissipation rate decay rapidly. Low values of k and ε are predicted anywhere else in the vessel. The turbulence kinetic energy is weak even in the

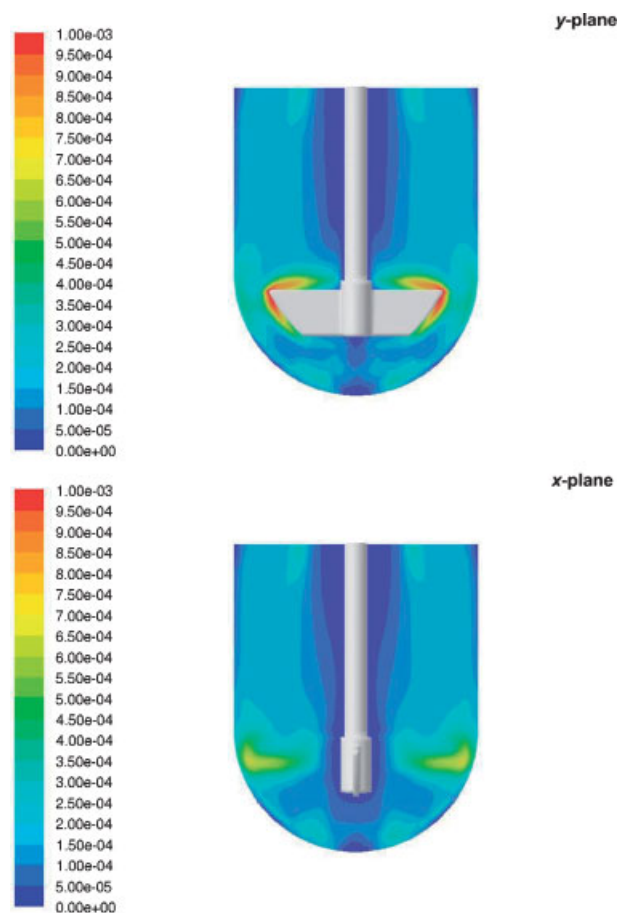


Figure 15. CFD predictions of the turbulence kinetic energy on vertical cross sections through the impeller shaft at different orientations (m^2/s^2).

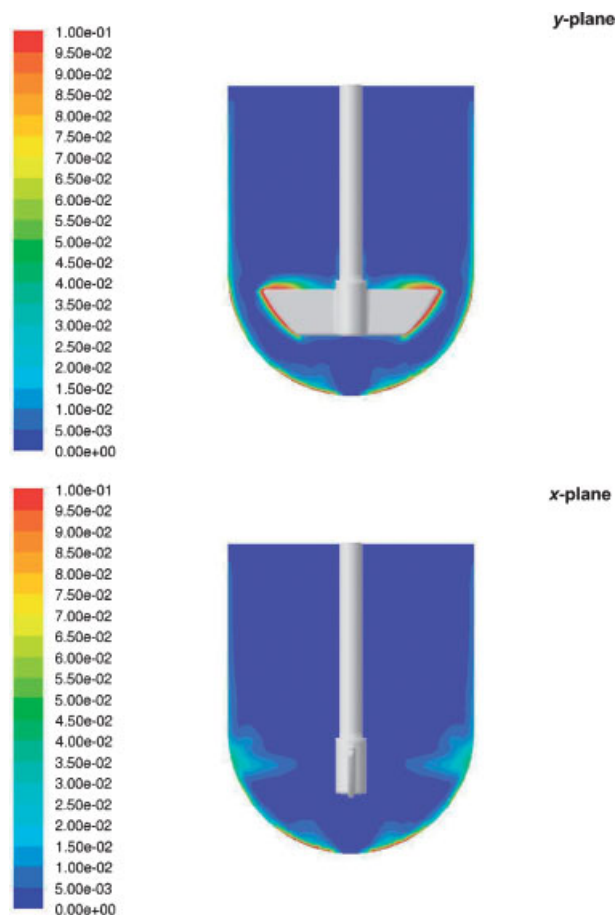


Figure 16. CFD predictions of the energy dissipation rate on vertical cross sections through the impeller shaft at different orientations (m^2/s^3).

region below the impeller where tablet dissolution occurs. Some higher values of energy dissipation rate appear along the vessel bottom, but not in the center where the tablet is usually located during a test.

Strain Rate

Figures 17 and 18 present contour plots of the strain rate, respectively, on a full vertical cross section of the vessel and, magnified, in the bottom region. As one can expect, the strain rate is high near the impeller blades and near the walls, where the velocity must eventually become zero and the velocity gradients are large. However, the strain rate is significantly higher at the wall in the region near the vessel bottom than at the wall in the cylindrical section the vessel. This phenomenon can be attributed not only to the proximity to the impeller, but also to the presence

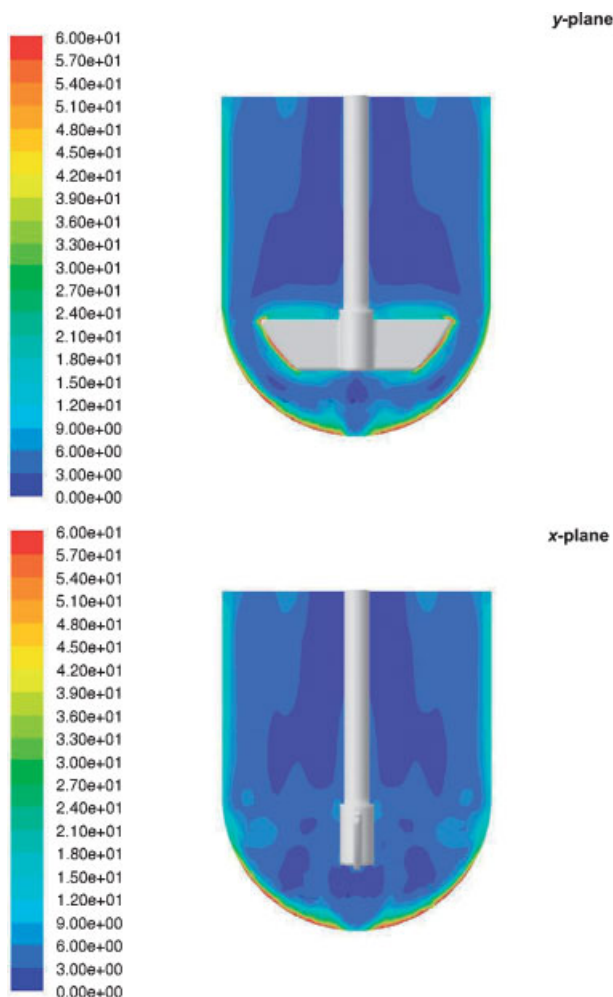


Figure 17. CFD predictions of strain rate on vertical cross sections through the impeller shaft at different orientations (1/s).

in this bottom region of steep velocity gradients resulting from the rapid variation in velocity magnitude over short distances, as indicated in the previous section.

The strain rate is not uniform in the region below the impeller. Figure 18 shows that the strain rate changes by more than an order of magnitude as one moves along to the hemispherical wall where the tablet is located during the dissolution test.

DISCUSSION

This is possibly the first study aimed at completely characterizing the hydrodynamics of a USP Dissolution Apparatus II through CFD simulations and a detailed point-by-point

comparison of the CFD predictions with experimental LDV data obtained for the entire dissolution vessel. Some of the results of this work can be compared with those of the few investigations available to date.

The results found here can be partially compared with those of Bocanegra et al.,⁹ who obtained LDA data for only a few selected locations in the dissolution vessel. The tangential velocities found here at two iso-surfaces ($z = -43.75$ mm and $z = 25$ mm) agree well with the experimental results of those authors.

A different group of investigators^{12,13,17} conducted a series of experimental studies using PIV and compared their data with CFD predictions. Because of the nature of their experimental data, these authors only produced a qualitative comparison between data and numerical predictions. However, their velocity plots appear to compare favorably with the detailed results obtained here.

Finally, another group of investigators^{18,19} used a CFD approach similar to that used here, but generated no experimental data of their own. Instead, they used the limited experimental data of Bocanegra et al.⁹ to partially validate their approach. A comparison of the results of McCarthy et al.¹⁹ with those obtained here shows that the basic features of the flow field in the vessels, such as the main recirculation patterns and the jet flowing inwards near the vessel bottom, are similar. However, some differences can be found in the finer flow structures. For example, the flow that was predicted and experimentally validated here for the innermost core in the upper region of the vessel is weaker than that which McCarthy et al. obtained. Their results also show intermediate recirculation patterns near the wall in the upper portion of the vessel, which were neither predicted nor experimentally measured here. In this regard, the results of Kukura et al.^{12,17} and Baxter et al.¹³ are more similar to those found here. A more interesting difference between the results of McCarthy et al.¹⁹ and those of the present work is in the finer flow structure below the impeller. McCarthy et al.¹⁹ found a stronger and much more structured “wavy” flow below the impeller than that numerically predicted here or reported by Kukura et al.^{12,17} and Baxter et al.¹³ Our experimental results seem to confirm that the flow below the impeller is indeed very weak in any direction other than tangential, and that the CFD predictions generally overestimate the intensity of such a flow. It should be stressed that the $k-\omega$

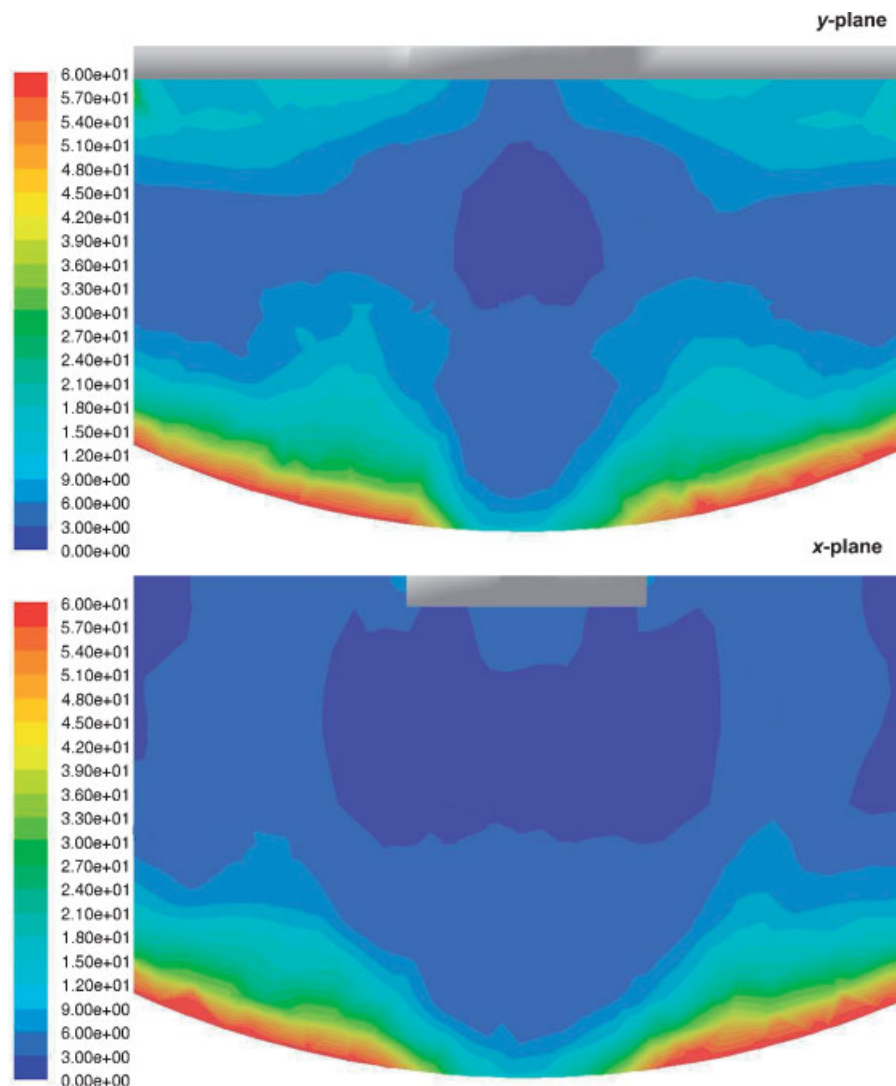


Figure 18. CFD predictions of the strain rate on vertical cross sections through the impeller shaft at different orientations for the bottom region (1/s).

model with low Reynolds number correction was used here to model turbulence effects. This model is probably superior to other standard turbulence models routinely used in simulations.^{26,27} However, it is unclear what turbulence model McCarthy et al.¹⁹ used in their work.

In general, the CFD predictions obtained here agreed reasonably well with the LDV data. This is important to validate the CFD results obtained in this work, and draw more wide-ranging conclusions based on them. In addition, the agreement indicates that the turbulence model used in this work, that is, the $k-\omega$ model with low Reynolds number correction, is appropriate for this kind of systems.

The hydrodynamics of the USP Apparatus II is dominated by two main features. The first is that anywhere in the system the main flow is strongly tangential, as in all unbaffled systems, with limited axial and radial components. Secondary flows are also present, but they form two smaller recirculation loops above and below the impeller. This has implications for the axial homogeneity of the vessel, although the small size of the vessel implies that blending is likely to occur relatively rapidly.

The second important hydrodynamic feature is that the central core region between the bottom of the vessel and the lower edge of the impeller is characterized by exceedingly small radial and

axial velocities and turbulence levels. This zone rotates with the impeller, and it is surrounded by another zone, also below the impeller, with much higher radial and axial velocities. This analysis can qualitatively explain the effect of “coning” at the center of the vessel bottom. Coning is often observed when a tablet disintegrates rapidly during the dissolution test, and the resulting granules form a rotating cone of loosely aggregating particles under the impeller.

The high degree non-uniformity in the flow field near the vessel bottom can introduce a degree of uncertainty in the dissolution test. A tablet that is dropped into the gently agitated liquid in the vessel, as in a typical dissolution test, may land at a random location on the vessel bottom, and thus be exposed to very different flow fields depending on its final position. The velocities in this region, albeit small, change significantly over short distance along the vessel bottom. This implies that small variations in the location of the tablet on the vessel bottom caused by the randomness of the tablet descent through the liquid are likely to result in significantly different velocities at the tablet location. The strain rate, which is another important factor that can affect the tablet dissolution rate, also changes significantly along the vessel bottom. The dramatic changes of both velocities and strain rate within a very small space can likely introduce variability in the dissolution test. Therefore, the vessel hydrodynamics and the initial location of the tablet after being dropped into the vessel can possibly affect the dissolution test results.

CONCLUSIONS

The following conclusions can be drawn from this work:

- The LDV measurements and the CFD velocity predictions are, in general, in substantial agreement
 - All tangential velocities, irrespective of where in the vessel they are obtained from, are oriented in the same direction as the impeller rotation, indicating a strong tangential flow. The highest tangential velocity is typically between 40% and 50% of the impeller tip speed on all iso-surfaces, both above and below the impeller.
 - The axial velocities are all significantly smaller than the tangential velocities, with magnitudes typically ranging between 0% and 15% of the tip speed. This implies that top-to-bottom recirculation in the USP II apparatus is weak, as in most unbaffled vessels. The radial velocities are even smaller than the tangential and axial velocities.
- The flow in the region below the impeller is complex, and it is strongly dominated by the tangential component while the radial and axial components are very weak. The presence of a vertical recirculation loop having a pulsating component generated by the passing of the impeller blades can be observed. When this pulsating effect decays, the flow is extremely weak.
 - In the region below the impeller, the vertical recirculation loop is not able to penetrate the inner core region located just under the shaft. The flow in this core is nearly quiescent in the vertical plane and is dominated by the tangential velocity. This weakly swirling but otherwise nearly stagnant core region extends all the way from the vessel bottom to the lower edge of the impeller. At its vertical boundaries, the axial velocities change rapidly with time and location, while remaining weak. This can explain the “coning” effect often observed at the center of the vessel bottom.
 - The strain rate is not uniform in the region below the impeller, but it changes by more than an order of magnitude by moving along the hemispherical bottom. This is likely to have an impact on the mass transfer rate and hence the dissolution rate, depending on the exact location of a tablet, or its deviation from it.

In conclusion, the hydrodynamics near the vessel bottom, where the tablet is located, can contribute to high variability in dissolution testing.

NOMENCLATURE

- D impeller diameter (m)
 k turbulence kinetic energy (m^2/s^2)
 G_k the generation of k due to mean velocity gradients ($\text{kg}/\text{m} \cdot \text{s}^3$)
 G_ω generation of ω ($\text{kg}/\text{m}^3 \cdot \text{s}^2$)
 N impeller rotational speed (rotations/s)

r	radial coordinate of LDV measurement point, (m or mm)
Re	impeller Reynolds number ($=\rho \cdot N \cdot D^2 / \mu$), dimensionless
S_k	user-defined source term of k ($\text{kg/m} \cdot \text{s}^3$)
S_ω	user-defined source term of ω ($\text{kg/m}^3 \cdot \text{s}^2$)
T	vessel diameter (m or mm)
u	velocity (m/s)
Y_k	dissipation of k ($\text{kg/m} \cdot \text{s}^3$)
Y_ω	dissipation of ω ($\text{kg/m}^3 \cdot \text{s}^2$)
z	vertical location of iso-surface (m or mm)

Greek Symbols

Γ_k	effective diffusivity of k ($\text{kg/m} \cdot \text{s}$)
Γ_ω	effective diffusivity of ω ($\text{kg/m} \cdot \text{s}$)
ε	turbulent dissipation rate (m^2/s^3)
μ	liquid viscosity ($\text{kg/m} \cdot \text{s}$)
ρ	liquid density (kg/m^3)
ω	specific dissipation rate (s^{-1})

ACKNOWLEDGMENTS

This work was supported through a grant from Merck & Co. West Point, PA, whose contribution is gratefully acknowledged. The authors also wish to thank Dr. Scott Reynolds for his contribution and support.

REFERENCES

1. The United States Pharmacopeia & The National Formulary. The Official Compendia of Standards, USP 29-NF 24 2005, Pharmacopial Convention, Inc., November 2005.
2. Moore JW, Flanner HH. 1996. Mathematical comparison of dissolution profiles. *Pharm Technol* 20:64–74.
3. Cohen JL, Hubert BB, Leeson LJ, Rhodes CT, Robinson JR, Roseman TJ, Shefter E. 1990. The development of USP dissolution and drug release standards. *Pharm Res* 7:983–987.
4. Mauger J, Ballard J, Brockson R, De S, Gray V, Robinson D, 2003. Intrinsic dissolution performance of the USP dissolution apparatus 2 (rotating paddle) using modified salicylic acid calibration tablets: Proof of principle. *Dissol Technol* 10:6–15.
5. Moore TW, Hamilton JF, Kerner CM. 1995. Dissolution testing: Limitation of USP prednisone and salicylic acid calibrator tablets. *Pharmaceutical Forum* 21:1387–1396.
6. Qureshi SA, McGilveray IJ. 1999. Typical variability in drug dissolution testing: Study with USP and FDA calibrator tablets and a marketed drug glibenclamide. *Product Europ J Pharm Sci* 7:249–258.
7. Qureshi SA, Shabnam J. 2001. Cause of high variability in drug dissolution testing and its impact on setting tolerances. *Europ J Pharm Sci* 12:271–276.
8. Costa P, Lobo JMS. 2001. Influence of dissolution medium agitation on release profiles of sustained-release tablets. *Drug Devel Ind Pharm* 27:811–817.
9. Bocanegra LM, Morris GJ, Jurewicz JT, Mauger JW. 1990. Fluid and particle laser Doppler velocity measurements and mass transfer predictions for USP paddle method dissolution apparatus. *Drug Devel Ind Pharm* 16:1441–1464.
10. Cox DC, Furman WB. 1982. Systematic error associated with Apparatus 2 of the USP dissolution test I: Effects of physical alignment of the dissolution apparatus. *J Pharm Sci* 71:451–452.
11. Cox DC, Furman WB, Thornton LK. 1983. Systematic error associated with Apparatus 2 of the USP Dissolution Test III: Limitation of Calibrators and the USP Suitability Test. *J Pharm Sci* 72:910–913.
12. Kukura J, Arratia PC, Szalai ES, Muzzio FJ. 2003. Engineering tools for understanding hydrodynamics of dissolution tests. *Drug Dev Ind Pharm* 29:231–239.
13. Baxter JL, Kukura J, Muzzio FJ. 2005. Hydrodynamics-induced variability in the USP Apparatus II Dissolution Test. *Int J Pharmaceutics* 292: 17–28.
14. FDC Reports. 2001. Recalls prompted by FDA on the increase. *The Gold Sheet* 35.
15. FDC Reports. 2002. Counterfeits pose special recall challenge. *The Gold Sheet* 36.
16. FDC Reports. 2003. Spike in potency-related problems contributes to overall rise in 2002 recalls. *The Gold Sheet* 37.
17. Kukura J, Baxter JL; Muzzio FJ. 2004. Shear distribution and variability in the USP Apparatus 2 under turbulent conditions. *Int J Pharmaceutics* 279:9–17.
18. McCarthy L, Bradley G, Sexton J, Corrigan O, Healy AM. 2004. Computational fluid dynamics modeling of the paddle dissolution apparatus: Agitation rate mixing patterns and fluid velocities. *AAPS Pharm Sci Tech* 5: Article 31.
19. McCarthy L, Kosiol C, Healy AM, Bradley G, Sexton J, Corrigan O. 2003. Simulating the hydrodynamic conditions in the United States pharmacopeias paddle dissolution apparatus. *AAPS Pharm Sci Tech* 4: Article 22.
20. Akiti O, Armenante PM. 2004. Experimentally-validated micromixing-based CFD model for fed-batch stirred-tank reactors. *AIChE J* 50:566–577.
21. Schäfer M, Höfken M, Durst F. 1997. Detailed LDV measurements for visualization of the flow field

- within a stirred-tank reactor equipped with a rushton turbine. *Chem Eng Res Des* 75:729–736.
22. Armenante PM, Chou CC, Hemrajani RR. 1994. Comparison of experimental and numerical fluid velocity distribution profiles in an unbaffled mixing vessel provided with a pitched-blade turbine. *ICHEME Symp Ser* 136:349–356.
 23. Armenante PM, Luo C, Chou CC, Fort I, Medek J. 1997. Velocity profiles in a closed unbaffled vessel: Comparison between experimental LDV data and numerical CFD predictions. *Chem Eng Sci* 52: 3483–3492.
 24. GAMBIT 2.2 User's Guide. 2005. Fluent, Inc. New Hampshire.
 25. FLUENT 6.2 User's Guide. 2005. Fluent, Inc. New Hampshire.
 26. Wilcox DC. 1998. *Turbulence modeling for CFD*. La Canada, California: DCW Industries, Inc.
 27. Hanjalic K, Nagano Y, Tummers M. 2003. *Turbulence Heat and Mass Transfer* 4. Redding, CT: Begell House, Inc. pp 625–632.
 28. Armenante PM, Chou CC. 1994. Experimental LDV measurement and numerical CFD determination of the fluid velocity distribution in an unbaffled mixing vessel. *AIChE Symp Ser* 90:33–40.
 29. Ciofalo M, Brucato A, Grisafi F, Torracca N. 1996. Turbulent flow in closed and free-surface unbaffled tanks stirred by radial impellers. *Chem Eng Sci* 51:3557–3573.
 30. Dong L, Johansen ST, Engh TA. 1994. Flow induced by an impeller in an unbaffled tank-I experimental. *Chem Eng Sci* 49:549–560.
 31. Dong L, Johansen ST, Engh TA. 1994. Flow induced by an impeller in an unbaffled tank-II numerical modeling. *Chem Eng Sci* 49:3511–3518.
 32. Murthy S, Jayanti S. 2002. CFD study of power and mixing time for paddle mixing in unbaffled vessels. *Chem Eng Res Des* 80:482–498.